

Study of flow rate induced measurement error in flow-through nano-hole plasmonic sensor

Long Tu, Liang Huang, Tianyi Wang, and Wenhui Wang^{a)}

*State Key Laboratory of Precision Measurement Technology and Instrument,
Department of Precision Instrument, Tsinghua University, Beijing, China*

(Received 27 September 2015; accepted 18 November 2015; published online 25 November 2015)

Flow-through gold film perforated with periodically arrayed sub-wavelength nano-holes can cause extraordinary optical transmission (EOT), which has recently emerged as a label-free surface plasmon resonance sensor in biochemical detection by measuring the transmission spectral shift. This paper describes a systematic study of the effect of microfluidic field on the spectrum of EOT associated with the porous gold film. To detect biochemical molecules, the sub-micron-thick film is free-standing in a microfluidic field and thus subject to hydrodynamic deformation. The film deformation alone may cause spectral shift as measurement error, which is coupled with the spectral shift as real signal associated with the molecules. However, this microfluid-induced measurement error has long been overlooked in the field and needs to be identified in order to improve the measurement accuracy. Therefore, we have conducted simulation and analytic analysis to investigate how the microfluidic flow rate affects the EOT spectrum and verified the effect through experiment with a sandwiched device combining Au/Cr/Si₃N₄ nano-hole film and polydimethylsiloxane microchannels. We found significant spectral blue shift associated with even small flow rates, for example, 12.60 nm for 4.2 μ l/min. This measurement error corresponds to 90 times the optical resolution of the current state-of-the-art commercially available spectrometer or 8400 times the limit of detection. This really severe measurement error suggests that we should pay attention to the microfluidic parameter setting for EOT-based flow-through nano-hole sensors and adopt right scheme to improve the measurement accuracy.

© 2015 AIP Publishing LLC. [<http://dx.doi.org/10.1063/1.4936863>]

INTRODUCTION

Ebbesen first experimentally discovered in 1998 the phenomenon of extraordinary optical transmission (EOT), which occurs when light is projected onto a noble metallic layer perforated with an array of periodic holes having a diameter smaller than the light wavelength.¹ The transmission spectrum is extremely sensitive to the hole structure (e.g., geometry and size) and surface properties of the metal layer (e.g., the dielectric constant). Though still a little controversial, EOT is widely thought to originate from surface plasmon resonance (SPR), and these EOT-associated nano-holes have been used as biochemical sensors to detect molecules that combine on the near-field (~ 200 nm distance) surface of nano-holes. These label-free sensors can be configured with collinear light paths and offer higher sensitivity compared to the traditional Kretschmann SPR configuration.^{1–7} Many researchers have succeeded in detecting biological molecules and the change of refractive index in solution based on the character of EOT.^{8–32} The most commonly used property of EOT is that its resonance peaks (there are a series of peaks in the optical transmission spectrum, which are produced at different interfaces) in the optical transmission spectrum would shift to long wavelength when the refractive index of medium at the metallic interface increases, and the red-shift amount is positively related to

^{a)} Author to whom correspondence should be addressed. Electronic mail: wwh@mail.tsinghua.edu.cn.

the change of refractive index. As refractive index is associated with species concentration (or dielectric function, density, etc.) but not species per se, EOT sensors can be often used for unspecific biochemical molecules detection.

According to the nano-holes' penetration degree, EOT sensors have two configurations: flow-over and flow-through. In the flow-over configuration, a thin (normally sub-400-nm thick), hybrid, and noble metal film, normally a layer of Au film on top of an adhesion Cr layer, is formed on a glass substrate. An array of periodic nano-holes are formed through only the hybrid thin Au/Cr film and dead-ended on the substrate. The solution containing analytes flows over these holes and thus the name flow-over. In the flow-through configuration, the substrate under the nano-holes and their vicinity (i.e., some no-hole region) is removed, leaving the suspended region of the thin film free-stand in the solution while the surrounding region anchored on a substrate, which is normally a Si wafer. To be compatible with the fabrication processes, a supporting film (Si_3N_4), also equivalently perforated with periodic nano-holes, is formed under the Au/Cr hybrid film to enhance its strength. Compared to flow-over sensors, flow-through sensors can greatly shorten the biosensing analysis time and simultaneously gather analytes.^{33,34} Since its introduction in 2008, the flow-through configuration has shown great promise in the biochemical detection field.^{35–37} Besides, flow-through nano-hole array also can function as nanofluidic channels in many exciting applications such as DNA and RNA translocation and profiling.^{38–41}

Despite its clear superiority, the free-standing flow-through nano-hole array thin film, normally operating in a fluidic field, is certainly subject to mechanical deformation, which alone presumably induces EOT spectral change as EOT is highly sensitive to the structure of nano-holes. This fluidic field induced spectral change, though not caused by the change of analytes (i.e., dielectric function), has long been blindly recorded in the measurement signal. This measurement process can be modeled as $s = s_0 + e_f + e_e$, where s is the measurement signal, s_0 is the true signal associated with the analyte, e_f is the error signal caused by the fluidic field, and e_e is all other error signals. As a source of measurement error, e_f is coupled with the true signal and needs to be quantitatively investigated in order to improve the measurement accuracy in biochemical detection. Therefore, we have systematically studied the effect of microfluidic field on the EOT spectral shift that happens to a free-standing gold film perforated with periodically arrayed nano-holes. Through simulation and experimental verification, we found that e_f/s_0 can be up to 8400 for even a low flow rate in microfluidics, indicating significantly severe measurement error caused by the microfluidic field. For the first time, we have developed the method to quantify the microfluidic field induced EOT spectral change and found significant measurement error for ultralow-volume analytes. This suggests extra care is needed for high-precision biochemical detection scenarios.

The rest of the paper is structured as follows. First, we describe the experimental setup and core devices for simulation and experiment. We then present the simulation to clarify the relationship between the pressure drop and the volume flow rate through those nano-holes. Next, we explain how to calculate the deformation of the thin film in relation to the pressure drop. Using the nano-hole structure model associated with the calculated deformation, we then show through finite-different time-domain (FDTD) simulation how the deformation or flow rate affects the EOT spectral shift, followed by the experimental results that verify the simulation results. Finally, we interpret the results and conclude the paper.

EXPERIMENTAL SETUP AND DEVICES

The experimental setup and devices for simulation and experiment are sketched in Fig. 1(a). The micro and nano devices used in the experiment include (i) the optically thick gold film perforated with nano-holes, and (ii) polydimethylsiloxane (PDMS) microchannels, as shown in Figs. 1(b)–1(d). The entire experiment setup is mainly based on a standard inverted microscope (Nikon, TE2000), and the optical setup is as follows: the filtered white light radiated from tungsten-halogen lamp is condensed by a microscope objective and then illuminates the nano-hole array from above. The light transmitted through the nano-hole array is then

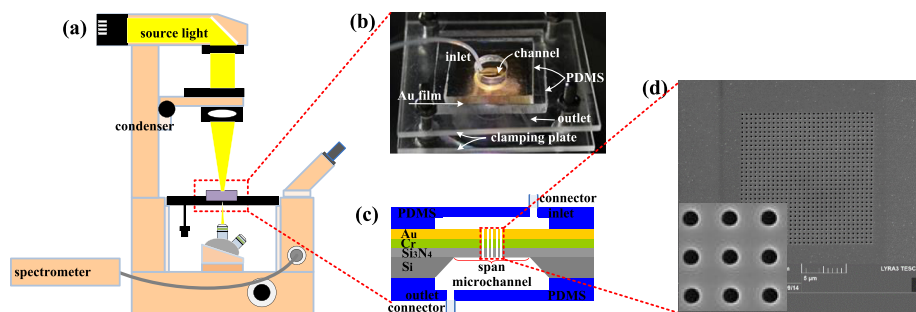


FIG. 1. Experimental setup and core devices. (a) Schematic of the optical microscopy setup and device for spectrum measurement. Note: The light beam is indicated in yellow just for visualization purpose, actually white light is projected on the device. (b) Image of the integrated device. (c) Section view of the integrated device structure. The film span is $940\ \mu\text{m}$ for our device. Dimensions not to scale. (d) SEM of 30×30 nano-holes (periodicity $500\ \text{nm}$, diameter $200\ \text{nm}$).

collected via the $10\times$ objective. The microscopic imaging system converges the light on the imaging focal plane of a C-mount side port, which is connected to a fiber optic spectrometer (Ocean Optics QE65Pro) for spectrum measurement. The preset volume flow rate is controlled by a syringe pump (Legato 200), which drives the flow in and out of the microchannels and nano-holes through the fluidic connectors. The experiment is performed at room temperature (25°C constant), and the influence of temperature on the deformation of free-standing Au/Cr/ Si_3N_4 film is minimized and ignored.

We determined the periodicity, a key parameter, of nano-holes before fabricating the nano-device. According to Ebbesen's theory,¹ when the incident light is normal to the periodic nano-hole array plane, the EOT resonance peak wavelength (λ_{max}) is given by

$$\lambda_{\text{max}} = \frac{P}{\sqrt{i^2 + j^2}} \sqrt{\frac{\epsilon_m \epsilon_d}{\epsilon_m + \epsilon_d}}, \quad (1)$$

where P is the periodicity of holes, integers (i, j) represent the Bragg resonance orders, ϵ_m and ϵ_d are the dielectric functions of the metal film and medium, respectively. We calculated the resonance peak wavelength based on Equation (1) and finally chose the nano-hole array's periodicity of $500\ \text{nm}$ to ensure the resonance peak wavelength located in the visible light range, which facilitates the observation and the detection by the spectrometer available in our lab.

The fabrication process of the nano-hole chip was described in detail in others work^{34,36} and is thus only briefed here for completeness. First, a $150\ \text{nm}$ -thick low-stress Si_3N_4 layer is deposited on both sides of a $400\ \mu\text{m}$ -thick (100) Si wafer by low pressure chemical vapor deposition (LPCVD). Second, a $1500\ \mu\text{m} \times 1500\ \mu\text{m}$ corrosion window is formed by reactive ion etching (RIE) one side of the wafer. Then, anisotropic Si wet etching process with potassium hydroxide (KOH) is performed from the corrosion window, leaving a free-standing layer of Si_3N_4 with a square span of $940\ \mu\text{m} \times 940\ \mu\text{m}$, as shown in Fig. 2. Next, a $10\ \text{nm}$ -thick Cr adhesion layer and $150\ \text{nm}$ -thick Au layer are deposited sequentially by electron-beam evaporation on the upside of the Si_3N_4 layer. Finally, a 30×30 nano-hole array is fabricated by milling through the free-standing Au/Cr/ Si_3N_4 layer with a focused ion beam (FIB), with the diameter and periodicity of the nano-holes being, respectively, $200\ \text{nm}$ and $500\ \text{nm}$. Fig. 1(d) presents the SEM image of the flow-through nano-hole array.

To facilitate the microfluidic interfacing with nano-holes, we fabricated two PDMS layers with microchannels by standard soft lithography.⁴² Basically, the two PDMS layers each have a $5\ \text{mm} \times 4\ \text{mm} \times 0.17\ \text{mm}$ chamber which spans a greater area than the nano-hole footprint and the corrosion window, respectively. As this fabrication process is fairly standard and simple, we omit it here. Once we have the nano-device and PDMS devices, we sandwich the nano-hole chip by the two PDMS layers. The sandwiched parts are tightly bonded together by degassing, and a home-made fixture is used to mechanically clamp the three components to avoid fluid

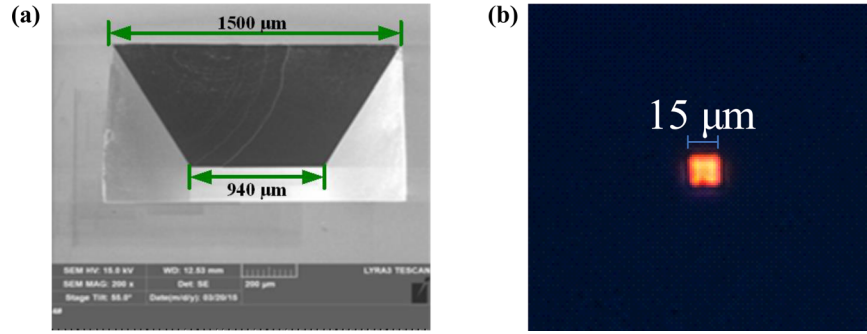


FIG. 2. Fabricated nano-device. (a) SEM picture of the free-standing Au/Cr/Si₃N₄ film anchored on (100) silicon wafer. The nano-device is placed upside down so that the correction window and the film span are visible. (b) Optical microscopic picture of the nano-hole array under the experiment illumination. The transmitted light color different from the incident white light indicates the happening of EOT.

leakage. Finally, an inlet and outlet are punched on both PDMS layers to allow solution connection via tubing with the external syringe pump.

PRESSURE DROP RELATED TO FLOW RATE

On the basis of the experiment device, we first studied the pressure drop across the porous Au/Cr/Si₃N₄ film in order to further calculate the film deformation. Darcy's law is normally used to describe the fluid flow through a porous medium. For the nano-holes which are supposed to have a circular section, by applying Darcy's Law, we can obtain the relationship between the pressure drop and the volume flow rate as⁴³

$$Q = \frac{\pi N r_o^4 p}{8 \mu L}, \quad (2)$$

where Q is the volume flow rate, p is the pressure drop, r_o is the radius of a single hole, μ is the dynamic viscosity of fluidic medium, L is the film thickness, and N is the number of holes.

To further verify Darcy's law, we conducted simulations in COMSOL. As the fluid continuity hypothesis and Navier-Stokes equation apply to fluid flow in microfluidic chips,^{44,45} the laminar flow model contained in COMSOL is confirmed to hold because the Reynolds number is calculated as much below 2000, which is the condition for a flow to be laminar. In our simulations, we used four orders of magnitude of span size. For each span size, we set four representative volume flow rates of 0.06 $\mu\text{L}/\text{min}$, 0.6 $\mu\text{L}/\text{min}$, 6.0 $\mu\text{L}/\text{min}$, and 60 $\mu\text{L}/\text{min}$. Fig. 3 depicts the pressure drop distribution across the span region for the case where the span is 50 μm . Other span (20 μm , 40 μm , and 100 μm) has the same pattern in that the pressure distribution over the entire span is nearly uniform regardless of holes or not. This result allows us taking the mean pressure drop over the entire span as the nominal pressure drop.

We summarize the pressure drop vs volume flow rate by COMSOL and its comparison with the value calculated by Darcy's law in Table I. The acceptable agreement between the calculation and the simulation validates the suitability of Darcy's law in nano-hole array fluidic mechanics. Then, we plot the data points in Fig. 4 and found the pressure drop is linear to the volume flow rate. More importantly, the linear relationship is irrelevant to the free-standing film's span in view of the four highly overlapping lines, which allows us safely using a model with a much smaller span size to proceed or otherwise fail due to the heavy computation burden with a greater size in simulation of the pressure drop. Therefore, in this paper, we obtained the pressure drop for the span of 940 μm by simulating a span of 50 μm .

ROTATION ANGLE ASSOCIATED WITH THE FILM DEFORMATION

Next, we calculated the deformation rotation angle associated with the film deformation caused by the pressure drop applied to the film. To do so, referring to Fig. 5, we assumed the film is

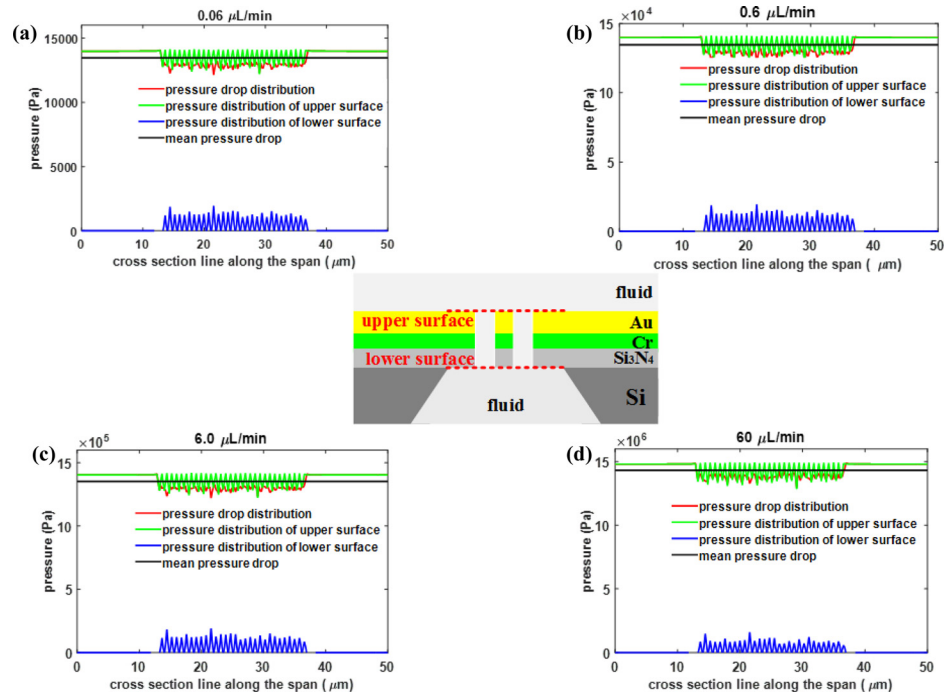


FIG. 3. Pressure distribution over the free-standing film when the film span is $50\ \mu\text{m}$. Here, the pressure distribution is plotted along the middle cross section of the film span, for the volume flow rate of $0.06\ \mu\text{L}/\text{min}$ (a), $0.6\ \mu\text{L}/\text{min}$ (b), $6.0\ \mu\text{L}/\text{min}$ (c), and $60\ \mu\text{L}/\text{min}$ (d). The pressure drop distribution is obtained by subtracting the lower surface's pressure distribution from the upper surface's pressure distribution.

mechanically homogeneous in-plane. And the individual cylindrical holes are uniformly deformed with the apex shrunk and the base expanded with respect to its half-height. Thus, the aperture of the cone is double the rotation angle of the deformed film. For the sub-micron-thick thin films, classical materials mechanics equations fail to describe the mechanical behavior, and Vlassak and Nix⁴⁶ proposed an analytic solution which was verified by their experiment. We therefore adopt it here as

$$p = \frac{c_1 \sigma_0 t h}{a^2} + \frac{c_2 E t h^3}{a^4}, \quad (3)$$

TABLE I. Comparison of the pressure drop values given by COMSOL simulation and Darcy's law for four orders of magnitude of film spans. Darcy's law gives a value approximately 60% of the simulated irrespective of the film span, showing good agreement and consistency.

Volume flow rate ($\mu\text{L}/\text{min}$)		0.06	0.6	6.0	60.0
Span $20\ \mu\text{m}$	Calculated (c) (Pa)	8.49×10^3	8.49×10^4	8.49×10^5	8.49×10^6
	Simulated (s) (Pa)	1.40×10^4	1.40×10^5	1.40×10^6	1.48×10^7
	Ratio (c/s) (%)	60.6	60.6	60.6	57.4
Span $40\ \mu\text{m}$	Calculated (c) (Pa)	8.49×10^3	8.49×10^4	8.49×10^5	8.49×10^6
	Simulated (s) (Pa)	1.30×10^4	1.30×10^5	1.31×10^6	1.39×10^7
	Ratio (c/s) (%)	65.3	65.3	64.8	61.1
Span $50\ \mu\text{m}$	Calculated (c) (Pa)	8.49×10^3	8.49×10^4	8.49×10^5	8.49×10^6
	Simulated (s) (Pa)	1.34×10^4	1.34×10^5	1.35×10^6	1.43×10^7
	Ratio (c/s) (%)	63.4	63.4	62.9	59.4
Span $100\ \mu\text{m}$	Calculated (c) (Pa)	8.49×10^3	8.49×10^4	8.49×10^5	8.49×10^6
	Simulated (s) (Pa)	1.38×10^4	1.38×10^5	1.39×10^6	1.47×10^7
	Ratio (c/s) (%)	61.5	61.5	61.1	57.8

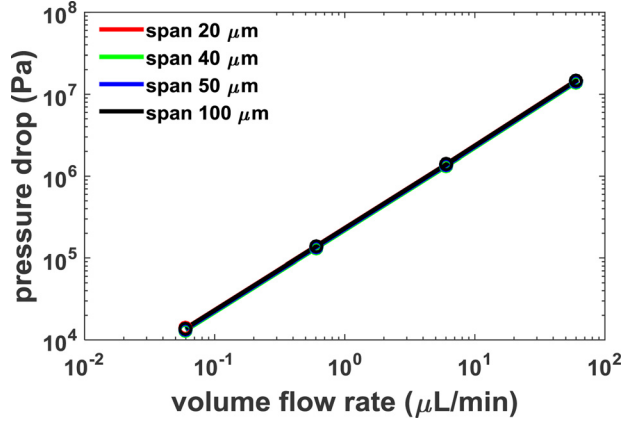


FIG. 4. Logarithmic graph of the pressure drop across the porous film vs volume flow rate through nano-holes for different free-standing film spans. The four fitting lines ($R^2 = 1$) are almost identical, indicating the pressure drop is almost irrelevant to the free-standing film's span.

where σ_0 and E are the residual stress and Young's modulus, respectively, c_1 and c_2 are the constants that depend on the aspect ratio of thin film, $2a$ is the span of thin film, t is the thickness of thin film, h is the deflection of thin film, and p is the pressure drop acting on the thin film.

As the residual stress of LPCVD silicon nitride and gold film is relatively small compared with their Young's modulus, the first term of Equation (3) can be neglected, and Equation (3) can be simplified as

$$p = \frac{c_2 E t h^3}{a^4}. \quad (4)$$

Based on the defined symbols, the deformation rotation angle θ is given by

$$\tan \theta = \frac{h}{a} = \sqrt[3]{\frac{pa}{c_2 E t}}. \quad (5)$$

It can be seen that the rotation angle is increasingly related to the pressure drop across the film and the span of the film, decreasingly related to the thickness of the film and the Young's modulus of the material. In this paper, the free-standing Au/Cr/Si₃N₄ film is composed of three layers of different material, including the 150 nm-thick gold film, the 10 nm-thick Cr film, and the 150 nm-thick LPCVD Si₃N₄ film. In calculation of the rotation angle, the 10 nm-thick Cr adhesion film can be omitted in the deformation analysis for its small thickness. We then

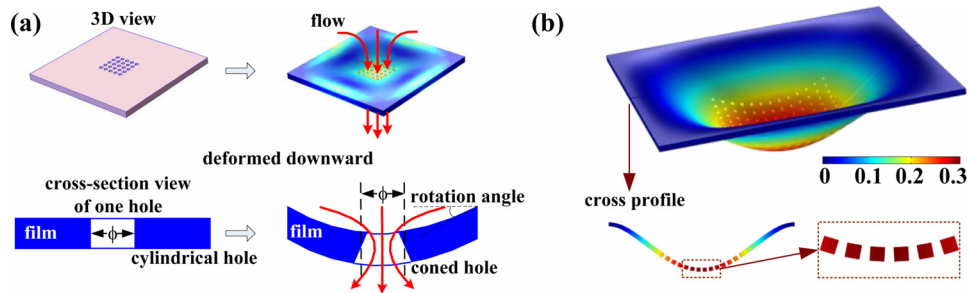


FIG. 5. Illustration of the free-standing nano-hole film subject to deformation under pressure drop. (a) Schematic diagram of the mechanical model. The holes in the array are assumed to be deformed uniformly and each be mechanically homogeneous about its symmetric axis. (b) The simulation result for an example deformed film, which has 13×13 nano-holes and a $15 \times 15 \mu\text{m}$ span. The cross profile of the deformed film indicates the assumption in (a) holds. Note the deformation is exaggerated for better visualization.

calculated two “virtual” rotation angles as if the thin film was solely an Au or Si₃N₄ layer, and took their average value as the rotation angle, as below

$$\tan \theta = \frac{1}{2} \times \left(\sqrt[3]{\frac{ap}{c_{21}E_1t}} + \sqrt[3]{\frac{ap}{c_{22}E_2t}} \right), \quad (6)$$

where c_{21} and c_{22} are the c_2 constants for Au and Si₃N₄, respectively, E_1 and E_2 are the Young’s modulus for Au and Si₃N₄, respectively.

We then plot the deformation rotation angle of the hybrid film in relation to the pressure drop under variable thin film spans in Fig. 6, using Equation (6). As the pressure drop is linear to the volume flow rate (Equation (2)), the rotation angle relates to the flow rate in the same trend as the pressure drop.

SPECTRAL SHIFT SIMULATION AND EXPERIMENT RESULTS

To investigate the spectral shift associated with the rotation angle, simulation and experiment were conducted sequentially. We first use FDTD Solutions to simulate the transmittance of gold nano-hole array by taking cylindrical and coned hole (Fig. 7) as one unit of periodic holes in the geometry before and after deformation, respectively. FDTD Solutions are a 3D Maxwell solver which can analyze the interaction of light with wavelength scale complicated nano-structures. Briefly speaking, FDTD is a numerical analysis and time-domain method used for modeling computational electrodynamics. By using the leap frog algorithm, the time-dependent and discretized Maxwell’s equations are repeatedly solved until the steady-state electromagnetic field behavior is fully evolved.⁴⁷ The gold nano-hole array structural parameters in FDTD simulation are set equal to the practical fabrication parameters. The boundary conditions for x axis and y axis are anti-symmetric and symmetric, respectively, and boundary conditions for z axis are perfectly matched layer (PML). The mesh grid is non-uniform, and grid step is 10 nm. Note here we assumed all the coned holes are within a flat (non-deformed) film, which is reasonable as the $15 \mu\text{m} \times 15 \mu\text{m}$ nano-hole array’s footprint is relatively small with respect to the $940 \mu\text{m} \times 940 \mu\text{m}$ free-standing thin film span under fluid pressure drop. According to Equation (6), the $940 \mu\text{m}$ span free-standing thin film’s equivalent rotational angle for the volume flow rate of $0.6 \mu\text{l/min}$, $1.8 \mu\text{l/min}$, $3.0 \mu\text{l/min}$, and $4.2 \mu\text{l/min}$ is, respectively, 4.8° , 6.9° , 8.2° , and 9.2° . In this way, we obtained the simulated spectrum vs rotation angle by FDTD (Fig. 8(a)) when water interfaces with gold and found that the thin film’s deformation under growing fluid volume flow rate increasingly causes spectral blue-shift. In particular, the (1, 0) resonance mode peak wavelength corresponding for Au-water interface shifts prominently towards short wavelength when the rotation angle or the equivalent volume flow rate increases. This trend agrees with previous research results in that the wavelength peak is blue-shifted as the coned holes have an increasing aperture angle.⁴⁸

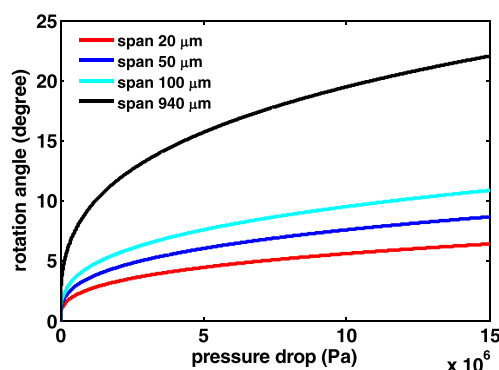


FIG. 6. The calculated rotation angle of the deformed film in response to pressure drop for different free-standing film spans. Here, we assume the film deforms within its elastic range, which was validated in experiment.

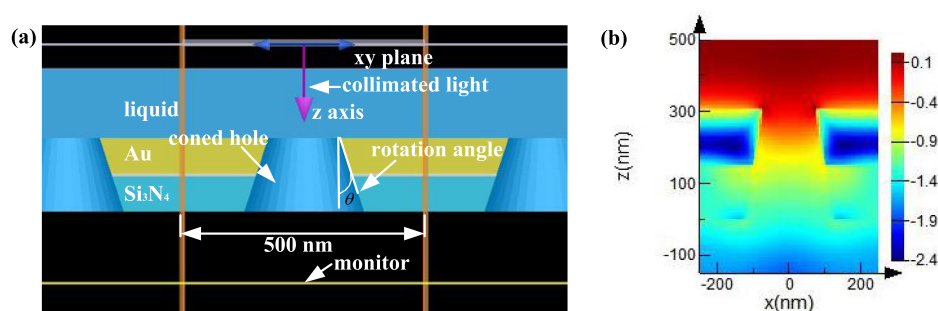


FIG. 7. (a) Schematic diagram of FDTD simulation model for the coned hole. (b) The electrical field intensity distribution for one coned hole.

We further verified this blue-shift via experiment (Fig. 8(b)) using the assembled setup. Before experiment, we FIB fabricated free-standing nano-hole Au/Cr/Si₃N₄ film and template-replicated PDMS microchannels as described previously. The PDMS microchannels were cleaned in an ultrasonic bath and dried in the clean room. The microchannels were rendered hydrophilic by oxygen plasma treatment. The nano-device was treated by ethanol and thoroughly washed by deionised (DI) water, followed by drying in the clean room. The two PDMS layers with microchannels were aligned and tightly assembled with the nano-device by

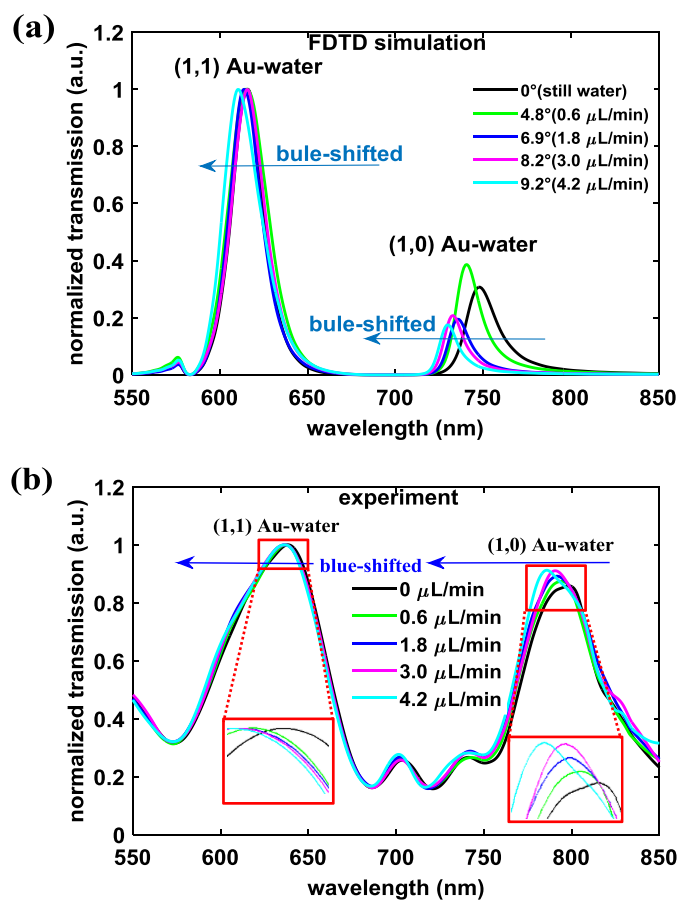


FIG. 8. EOT transmission spectrum vs volume flow rate. (a) FDTD simulated result. (b) Experimental result. Note the film span is $940\ \mu\text{m}$ for both simulation and experiment. The experiment was conducted under constant conditions except varying flow rate.

TABLE II. Comparison of the simulated and measured Au-water (1, 0) peak transmission wavelength. The spectral blue-shift with respect to still water increases as the volume flow rate.

Volume flow rate ($\mu\text{l/min}$)		0	0.6	1.8	3.0	4.2
Simulation (s)	Peak (nm)	748.26	740.88	735.43	732.74	730.07
	Shift (nm)	0	-7.38	-12.83	-15.52	-18.19
Experiment (e)	Peak (nm)	798.57	794.37	791.58	790.52	785.97
	Shift (nm)	0	-4.20	-6.99	-8.05	-12.60
Spectral shift ratio (e/s) (%)		...	56.9	54.5	51.9	69.3

degassing and mechanically clamping to form a hybrid micro-nano-device. Then, two connecting holes were punched through the PDMS layers and connected to the syringe pump for fluid control.

In experiment, initially DI water was infused to the microchannels and nano-holes by gravity. This slow infusion of medium filled up the channel space of the device, so no air bubbles troubled the experiment. Then, we used the syringe pump to drive DI water using the same volume flow rate of 0.6 $\mu\text{l/min}$, 1.8 $\mu\text{l/min}$, 3.0 $\mu\text{l/min}$, and 4.2 $\mu\text{l/min}$ as used in simulation. The maximum flow rate used here allowed the film working in its elastic range without rupture or burst observed. Furthermore, we confirmed this by observing the spectrum return to its original shape after the volume flow rate was set back from 4.2 $\mu\text{l/min}$ to 0 $\mu\text{l/min}$. For each flow rate, the syringe pump maintained the rate for enough time to allow the medium reaching steady state, where the spectrometer was launched to record the spectrum signal. The spectrometer's integral time was set 10 s, and the raw spectrum data were exported to MATLAB and processed by the lossless smooth method to remove signal fluctuations. Then, the background spectrum was removed from the signal spectrum, and the resultant spectrum was divided by light source's spectrum to obtain the transmittance spectrum, which was individually normalized with respect to its own peak intensity.

The data summarized in Table II show the flow rate caused spectral blue-shift in both experiment and simulation, increasingly and enormously. The experimental results are about 50%–70% simulation results, showing good agreement with the trend of simulation results in the blue-shift associated with increasing volume flow rate. This confirms the feasibility of theoretical analysis, assumptions, and approximation for the thin film deformation, fluidic mechanics of nano-holes, and FDTD simulation. Compared to still water (zero flow rate), the (1, 0) resonance mode peak wavelength of Au-water interface was blue-shifted about 12 nm when the flow rate increased to 4.2 $\mu\text{l/min}$, which is generally low in microfluidics. This spectral shift corresponds to 90 times the optical resolution of the current state-of-the-art spectrometer like what was used (Ocean Optics QE65Pro) in our experiment. In measurement applications, by using some technique like averaging a large number of spectra,⁴⁹ the limit of detection (LOD, or the minimum effective signal to be detected) is $1.5 \times 10^{-3} \text{ nm}$, thus 12.60 nm spectral shift is equivalent to 8400 times LOD. Therefore, the wavelength blue-shift associated with the low flow rate like 4.2 $\mu\text{l/min}$ can be about 8400 times the true signal. From another perspective, this 12.6 nm blue-shift for 4.2 $\mu\text{l/min}$ is equivalent to 0.0252 refractive index units (RIU)⁵⁰ as the refractive index sensitivity of EOT based detection is usually around 500 nm/RIU. 0.0252 RIU in biochemical detection means a lot. For example, it is equivalent to the RIU difference between $\sim 17\%$ (w/w) sucrose solution or $\sim 40\%$ (w/w) ethanol solution and pure water. All these strongly indicate the severity of the blue-shift associated with the flow rate as measurement error, which cannot afford to ignore by any means.

DISCUSSION AND CONCLUSIONS

The spectra obtained through experiment exhibit the same patterns as the simulated. First, they have two paramount peaks in simulation and experiment, corresponding to the (1, 1) and

(1, 0) order resonance peak wavelength, respectively. Second, the spectra have the commonly reported feature of the asymmetry around the transmitted peaks. The minimum in the transmission curves corresponds to a diffraction phenomenon known as Wood's anomaly.³⁷ Differently from the simulation curves, however, the experimental spectra have two small peaks in between the two paramount peaks. The small peaks are produced by Au-Cr and Cr-Si₃N₄ interfaces⁵¹ and can be ignored in practice because they are little relevant to the medium to be measured. Note the Au-water (1, 0) resonance peak wavelength deviation between the simulation and experiment is relatively large. This can be seen from Figure 8 and Table II. Take the zero flow rate, for example, the peak occurred at 748.26 nm in simulation, while 798.57 nm in experiment. This ~50 nm deviation could be attributed to factors such as the size deviation in nano-hole milling and physical property (e.g., dielectric function) variation due to imperfect fabrication of the hybrid Au/Cr/Si₃N₄ thin film. Nevertheless, the resonance peak wavelength only works as the measurement baseline for calculating the spectral shift, so the deviation between experiment and simulation is not an issue.

In summary, we have systematically studied the microfluidic effect on the EOT spectral shift of free-standing nano-hole film and found significant spectral blue shift associated with the microfluidic flow rate through simulation and experiment. Even for low flow rate of 4.2 $\mu\text{l}/\text{min}$, the 12.6 nm blue-shift is two orders of magnitude of the sensing resolution of a spectrometer. Normally coupled with the measurement signal, this severe measurement error needs to be eliminated to improve the measurement accuracy. The important finding indicates that we should pay attention to the microfluidic parameter setting for EOT-based free-standing film sensors and adopt right scheme to improve the measurement accuracy. If the measurement process simply uses a constant flow rate, this error may be treated as systematic error, which can be easily eliminated by many existing methods such as using the sensor in differential mode. However, when the flow rate is not constant on demand or due to external disturbance, which is the case in many scenarios, the sensor needs to be calibrated by identifying the spectral shift for a range of operating flow rates. The approach reported in this paper can therefore play the key role in calibration and enable enhanced measurement accuracy for biochemical detection applications.

ACKNOWLEDGMENTS

This work was supported by the NSFC (Grant No. 61376120), the One-Thousand Young Talent Program of China, and the National Instrumentation Project (Grant No. 2013YQ19046701). The authors would also like to thank Dr. Mohamadreza Najiminaini and Mr. Oubo You for sharing FDTD simulation experience, Dr. Zhaoxin Geng and Dr. Baogang Quan for helpful discussion at the early stage of this work.

¹T. W. Ebbesen, H. J. Lezec, and H. F. Ghaemi *et al.*, *Nature* **391**(6668), 667–669 (1998).

²C. Genet and T. W. Ebbesen, *Nature* **445**(7123), 39–46 (2007).

³F. J. García-Vidal, L. Martín-Moreno, T. W. Ebbesen *et al.*, *Rev. Mod. Phys.* **82**(1), 729 (2010).

⁴L. Moreno and F. García-Vidal, *Opt. Express* **12**(16), 3619–3628 (2004).

⁵J. Ji, J. G. O'Connell, D. J. D. Carter *et al.*, *Anal. Chem.* **80**(7), 2491–2498 (2008).

⁶C. Escobedo, *Lab Chip* **13**(13), 2445–2463 (2013).

⁷L. Tu, W. Wang, and Z. Qiu, *Spectrosc. Spectral Anal.* **35**(3), 751–759 (2015).

⁸J. Choi, K. Kim, Y. Oh *et al.*, *Adv. Opt. Mater.* **2**(1), 48–55 (2014).

⁹J. Junesch, T. Sannomiya, and A. B. Dahlin, *ACS Nano* **6**(11), 10405–10415 (2012).

¹⁰N. J. Wittenberg, H. Im, T. W. Johnson *et al.*, *ACS Nano* **5**(9), 7555–7564 (2011).

¹¹S. G. Rodrigo, O. Mahboub, A. Degiron *et al.*, *Opt. Express* **18**(23), 23691–23697 (2010).

¹²A. A. Yanik, M. Huang, O. Kamohara *et al.*, *Nano Lett.* **10**(12), 4962–4969 (2010).

¹³M. Najiminaini, F. Vasefi, B. Kaminska *et al.*, *Opt. Express* **18**(21), 22255–22270 (2010).

¹⁴H. Im, A. Lesuffleur, N. C. Lindquist *et al.*, *Anal. Chem.* **81**(8), 2854–2859 (2009).

¹⁵J. S. Kee, S. Y. Lim, A. P. Perera *et al.*, *Sens. Actuators, B* **182**, 576–583 (2013).

¹⁶G. J. Kowalski, A. Talakoub, J. Ji *et al.*, *Opt. Eng.* **48**(10), 104402 (2009).

¹⁷E. Maeda, S. Mikuriya, K. Endo *et al.*, *Appl. Phys. Lett.* **95**(13), 133504 (2009).

¹⁸S. G. Rodrigo, F. J. García-Vidal, and L. Martín-Moreno, *Phys. Rev. B* **77**(7), 075401 (2008).

¹⁹T. I. Wong, S. Han, L. Wu *et al.*, *Lab Chip* **13**(12), 2405–2413 (2013).

²⁰C. Valsecchi and A. G. Brolo, *Langmuir* **29**(19), 5638–5649 (2013).

²¹J. P. Monteiro, L. B. Carneiro, M. M. Rahman *et al.*, *Sens. Actuators, B* **178**, 366–370 (2013).

- ²²F. Eftekhari, R. Gordon, J. Ferreira *et al.*, *Appl. Phys. Lett.* **92**(25), 253103 (2008).
- ²³A. De Leebeek, L. K. S. Kumar, V. de Lange *et al.*, *Anal. Chem.* **79**(11), 4094–4100 (2007).
- ²⁴N. C. Lindquist, A. Lesuffleur, H. Im *et al.*, *Lab Chip* **9**(3), 382–387 (2009).
- ²⁵S. H. Lee, T. W. Johnson, N. C. Lindquist *et al.*, *Adv. Funct. Mater.* **22**(21), 4439–4446 (2012).
- ²⁶N. J. Wittenberg, H. Im, X. Xu *et al.*, *Anal. Chem.* **84**(14), 6031–6039 (2012).
- ²⁷N. C. Lindquist, A. Lesuffleur, and S. H. Oh, *Phys. Rev. B* **76**(15), 155109 (2007).
- ²⁸A. Lesuffleur, H. Im, N. C. Lindquist *et al.*, *Appl. Phys. Lett.* **90**(24), 243110 (2007).
- ²⁹C. Escobedo, A. G. Brolo, R. Gordon *et al.*, *Nano Lett.* **12**(3), 1592–1596 (2012).
- ³⁰K. L. Lee, S. H. Wu, and P. K. Wei, *Opt. Express* **17**(25), 23104–23113 (2009).
- ³¹K. L. Lee, J. B. Huang, J. W. Chang *et al.*, *Sci. Rep.* **5**, 8547 (2015).
- ³²S. H. Wu, K. L. Lee, R. H. Weng *et al.*, *PLoS One* **9**(2), e89522 (2014).
- ³³H. Im, N. J. Wittenberg, A. Lesuffleur *et al.*, *Chem. Sci.* **1**(6), 688–696 (2010).
- ³⁴S. Kumar, N. J. Wittenberg, and S. H. Oh, *Anal. Chem.* **85**(2), 971–977 (2012).
- ³⁵F. Eftekhari, C. Escobedo, J. Ferreira *et al.*, *Anal. Chem.* **81**(11), 4308–4311 (2009).
- ³⁶C. Escobedo, A. G. Brolo, R. Gordon *et al.*, *Anal. Chem.* **82**(24), 10015–10020 (2010).
- ³⁷R. Gordon, D. Sinton, K. L. Kavanagh *et al.*, *Acc. Chem. Res.* **41**(8), 1049–1057 (2008).
- ³⁸C. Gupta, W. C. Liao, D. Gallego-Perez, C. E. Castro, and L. J. Lee, *Biomicrofluidics* **8**(2), 024114 (2014).
- ³⁹S. Liu, Y. Yan, Y. Wang, S. Senapati, and H. C. Chang, *Biomicrofluidics* **7**(6), 61102 (2013).
- ⁴⁰K. F. Lo and Y. J. Juang, *Biomicrofluidics* **6**(2), 26504 (2012).
- ⁴¹W. Ouyang and W. Wang, *Biomicrofluidics* **8**(5), 052106 (2014).
- ⁴²Y. Xia, E. Kim, X. M. Zhao *et al.*, *Science* **273**(5273), 347–349 (1996).
- ⁴³H. I. Ene and D. Poliwevski, *Thermal Flow in Porous Media* (Reidel, Dordrecht, 1987).
- ⁴⁴L. Bocquet and E. Charlaix, *Chem. Soc. Rev.* **39**(3), 1073–1095 (2010).
- ⁴⁵S. Arya, S. Khan, A. Vaid *et al.*, *J. Nano-Electron. Phys.* **5**(4), 04047 (2013).
- ⁴⁶J. J. Vlassak and W. D. Nix, *J. Mater. Res.* **7**(12), 3242–3249 (1992).
- ⁴⁷C. Schuster, A. Christ, and W. Fichtner, *Microwave Opt. Technol. Lett.* **25**(1), 16–21 (2000).
- ⁴⁸T. Søndergaard, S. I. Bozhevolnyi, S. M. Novikov *et al.*, *Nano Lett.* **10**(8), 3123–3128 (2010).
- ⁴⁹H. Im, J. N. Sutherland, J. A. Maynard *et al.*, *Anal. Chem.* **84**(4), 1941–1947 (2012).
- ⁵⁰G. A. C. Tellez, R. N. Tait, P. Berini *et al.*, *Lab Chip* **13**(13), 2541–2546 (2013).
- ⁵¹S. H. Lee, N. C. Lindquist, N. J. Wittenberg, L. R. Jordana, and S.-H. Oh, *Lab Chip* **12**, 3882–3890 (2012).